Available online at www.sciencedirect.com
ScienceDirect
Journal of the European Ceramic Society 31 (2011) 1257–1268
www.elsevier.com/locate/jeurceramsoc

Processing and microstructural study of surface laser remelted Al_2O_3–YSZ–YAG eutectic plates

F.J. Ester [a], A. Larrea, R.I. Merino *

Instituto de Ciencia de Materiales de Aragón, CSIC - Universidad de Zaragoza, Pedro Cerbuna 12, 50009 Zaragoza, Spain

Available online 16 September 2010

Abstract

Surface modification of ternary Al_2O_3–Zr_2O_3–Y_2O_3 eutectic oxides was produced by laser melting. Preheating the ceramics and using a protecting atmosphere, we obtained homogeneous eutectic surface layers of 7 mm × 25 mm and 400 μm thick. The remelted layers were dense using processing rates below 500 mm/h but showed bubble porosity at faster processing rates. The phases in the resultant material were cubic zirconia (YSZ), α-Al_2O_3 and $Y_3Al_5O_{12}$ (YAG). At 20 mm/h, the remelted layer presented a Chinese-script like microstructure formed by an interpenetrating network of Al_2O_3 and YAG. At travelling speeds greater than 500 mm/h colonies were formed. At the largest processing rates the microstructure becomes fibrous like, the YSZ phase locating at the interface between Al_2O_3 and YAG phases. The chemical composition was independent of position into the layer. The very fine microstructure allows an in-line optical transmittance in the NIR of 60% for a 380 μm thick layer processed at 3500 mm/h.

Keywords: Nanoceramics; Eutectics; Laser melting; Alumina; Zirconia; YAG

1. Introduction

Directionally solidified Al_2O_3-based eutectic ceramic oxides (DSECO) present good retention of mechanical properties at high temperature.[1] Moreover, its high chemical stability in the presence of aggressive environments and its high corrosion and oxidation resistance has brought about intensive research and development of new Al_2O_3-based ceramic oxides for high temperature structural applications. Eutectics of Al_2O_3/Y_2O_3/ZrO_2 system are the most studied, among which stand out the Al_2O_3/ZrO_2 binary systems.[2–6] Many works about the Al_2O_3/$Y_3Al_5O_{12}$ and Al_2O_3/ZrO_2 (Y_2O_3) eutectics have been performed during the last decade. The DSECO Al_2O_3/ZrO_2 (3 mol% Y_2O_3) has good mechanical properties at ambient temperature (high fracture toughness (4–5 MPa $m^{1/2}$)),[7,8] but its strength diminishes above 1500 °C which is associated with the release of the thermal residual stresses, and the activation of plastic deformation mechanisms at the microscopic level in the ZrO_2 phase.[1,3,5,9] On the other hand, the directionally solidified Al_2O_3/$Y_3Al_5O_{12}$ eutectic has better strength retention at high temperature. It has a flexural strength of 1.9 GPa at ambient temperature, and of 1.65 GPa at 1700 K. These mechanical properties at room temperature are the result of a fine microstructure, strong and clean interfaces between phases, while the presence of YAG, which presents a good resistance to dislocation motion, contributes to the high temperature retention of strength. However, although strong, the composite is a brittle material.[2]

A third composite, the ternary eutectic Al_2O_3/$Y_3Al_5O_{12}$/ZrO_2 (AYZ), presents better mechanical properties than the previous ones. At high growth speeds it presents a very fine and interpenetrated microstructure, of the order of hundreds of nm, without the formation of colonies.[10,11] This microstructure is finer than the one of binary alumina-based compounds, due to presence of ZrO_2 which makes more sluggish the liquid to three-phase ordered solid transition and reduces the growth length scale.[12] Moreover, the presence of ZrO_2 increases the fracture toughness with respect to Al_2O_3/$Y_3Al_5O_{12}$, since it acts as a deflection flaw element and introduces residual stresses.[13] By the laser floating zone (LFZ) method, Peña et al.[10] produced AYZ rods, that showed a fracture toughness of 4.3 MPa $m^{1/2}$ and a flexural strength at ambient temperature of 4.6 GPa[12] which is almost four times higher than the best results measured in bulk non-oxide ceramics, such as SiC and Si_3N_4,[3,4] and twice as high as the highest reported in directionally solidified eutectic oxides of the

* Corresponding author. Tel.: +34 976 761333; fax: +34 976 761229.
E-mail address: rmerino@unizar.es (R.I. Merino).
[a] At <fn0005>present: BSH Electrodomésticos España, S.A, Avda. de la Industria, 49, 50016 Zaragoza, Spain.

0955-2219/$ – see front matter © 2010 Elsevier Ltd. All rights reserved.
doi:10.1016/j.jeurceramsoc.2010.08.016

family $Al_2O_3/Y_2O_3/ZrO_2$. Therefore, the eutectic AYZ is the most promising material of the Al_2O_3-based eutectic ceramic oxides as it combines a fine microstructure with a reasonably high toughness.

Ceramics composed of different phases are of interest not only for their structural properties, but also as functional ceramics. In particular, as optical materials, one can take advantage of its multiphase nature to widen the laser tunability range, or to generate selective infrared (IR) to visible (VIS) upconversion.[14] For some of those applications, it would be desirable to decrease light scattering to a minimum to fabricate transparent or translucent ceramics. This is particularly true for its use in optical systems where the better mechanical response of ceramics with respect to crystals is required, or when cost-efficiency recommends ceramic technology for fabrication of the component, as in armour, lighting, scintillators or lasers.[15] At present, the best transmitting (in-line transmission) ceramics are obtained by optimum processing of nanograined fully dense ceramics,[16] which is not an easy task. Fine grained, dense ceramics can be also achieved by laser melting of eutectic ceramics.[12] The in-line optical transmission of microstructured eutectic ceramic will be surely smaller than the one of optimised single-phase ceramics as phases with different refractive indexes are present, however, their excellent mechanical properties together with the potentiality of its multiphase nature and the inherent transparency of the components advise studying them.

The fabrication-from-the-melt techniques subject the material to high thermal gradients and entails high thermal solidification stresses, particularly when submicrometer microstructures are to be obtained, which require large solidification rates. These ones use to produce fracture during processing or generate a macroscopic residual stress state. Another problem relevant to this material is the trapping of gas bubbles during processing.[17] This brings porosity into the layer which deteriorates the mechanical properties and can destabilize coupled eutectic growth. This is the reason why only small volumes of AYZ have been produced. To date, small diameter rods (of 1–2 mm diameter) or small thickness plates (of 0.5–1.5 mm thickness) have been produced by rapid solidification, micro-pulling-down or LFZ methods.[10–12,18,19] In all these cases, the samples are completely molten which do not permit producing big volumes of eutectic material.

Being able to produce bigger volumes or surfaces of eutectic AYZ, would allow studying particular mechanical properties where bigger areas are needed, as specific wear rate or flexural strength. Moreover, if the growth rate could be increased, the microstructure would be finer, and it would entail an improvement on the mechanical properties, associated to the decreased flaw size. Only recently, Su et al. have reported hypoeutectic 6 mm rods of laser remelted AYZ eutectics[20,21] with very fine microstructure. Laser assisted surface melting-and-solidification enables to melt macroscopic surfaces at high movement rates. This laser surface treatment has been recently investigated to produce crack-free densification of Al_2O_3-based refractories.[22] It has also been used to generate more wear resistant surface coatings on Al_2O_3/ZrO_2 (3% Y_2O_3) eutectic plates[23–25] and also tried with other oxide and non-oxide eutectic compounds.[26]

In this work laser surface melting will be applied to eutectic AYZ plates to produce dense layers on top of macroscopic samples processed up to a maximum movement rate of 3500 mm/h. The processing method and the main appearance of the layers are described. A detailed microstructural study of the samples has been done, and the influence of the growth rate in the processing of AYZ eutectics has been analysed. Layers of fine-microstructured ternary eutectic have been obtained, which show translucency in the VIS and NIR regions, even when the optical contrast between YSZ and the other phases is quite strong.

2. Experimental details

Ceramic plates with densities around 90% of the theoretical density were prepared using commercial powders by slip casting of aqueous suspensions with a solid content of 70 wt.%. The powder mixture was prepared using the following commercial powders: Y_2O_3 (Aldrich, 99%), α-Al_2O_3 (Ceralox HPA-0.5 C10214, 99.99%), YSZ (8 mol% Y_2O_3) (Tosho TZ-YS, 99.9%), and Mn_2O_3 (99% Aldrich) to get the composition close to the ternary eutectic point: 62.4 mol% Al_2O_3, 21.3 mol% ZrO_2, 15.59 mol% Y_2O_3, doped with 0.67 mol% Mn_2O_3. The Mn_2O_3 doping was intended to increase absorption of diode laser radiation by the ceramic. This composition gave rise, after solidification, to a homogeneous microstructure, free from primary or segregated crystals, at all used processing rates.

The powders were thoroughly mixed, dispersed and suspended in water using Duramax D-3005 (Rohm and Haas Company, Philadelphia, USA) as dispersant with a concentration of 0.8 wt.%, in reference to solids. The obtained suspension was ball milled with a planetary mill during 2 h before casting. The green compacts were dried overnight and pre-sintered at 1000 °C for 3 h, cut near to the final size, and finally sintered at 1520 °C for 5 h. The pieces were then carefully ground to rectangular prisms prior to laser surface processing. The samples were processed by laser surface melting as has been described elsewhere[24–26] using a focused diode laser line (Rofin DL-X50, $\lambda = 940 \pm 10$ nm) and preheating the samples.

Transverse cross-sections of the processed samples were cut from the prisms along planes perpendicular to the laser travelling direction, and prepared by diamond polishing in order to be observed in a scanning electron microscope (model 6400, Jeol, Tokyo, Japan). The microscope was equipped with an X-ray detector from Oxford Instruments for energy dispersive X-ray analysis. This was used for chemical analysis using pure substances as calibrants. The microstructure of the fast remelted samples was examined by transmission electron microscopy. Transverse cross-sections were cut and mechanically thinned down to 40 μm, ion-milled at 77 K and carbon coated. They were observed in a Jeol 2000FXII microscope equipped with an INCA 200 X-ray microanalysis detector. X-ray diffraction experiments were carried out using a Rigaku D-Max system. Step-scanned patterns were measured between 10° and 90° (in

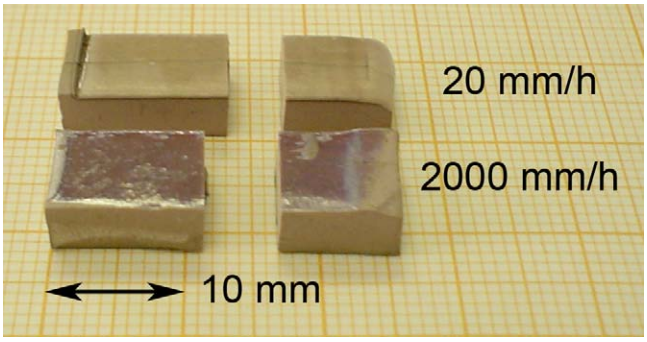

Fig. 1. Optical micrographs of transverse sections of samples processed at travelling speeds of 20 mm/h (up) and 2000 mm/h (down).

steps of 0.03) at room temperature. Raman spectroscopy measurements were made at room temperature and 77 K using an optical spectrometer (Model XY, DILOR, Lille, France) with a CCD detector. We used an Ar^+ laser as excitation source. Optical transmission of polished slabs was measured on a Cary 500 Scan UV-VIS-NIR spectrophotometer.

3. Laser surface melting

Rectangular prism samples of dimensions 25 mm × 7 mm × 5 mm (length × width × depth) were placed on top of a plate which was heated to 1100 °C. Preheated dry N_2 was blown into this heating stage that had a SiO_2 glass window

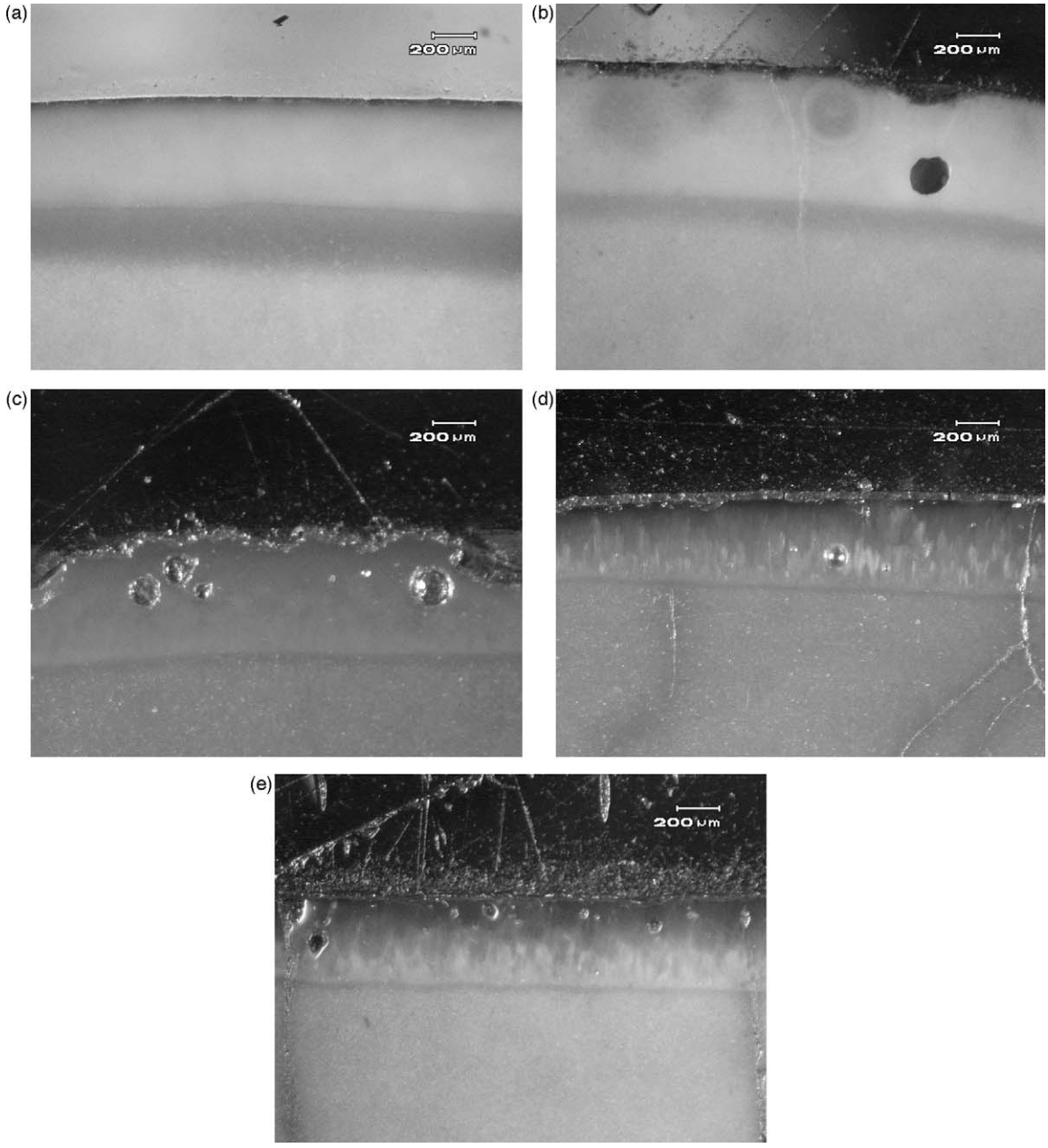

Fig. 2. Optical transverse cross-sections of samples processed at different rates. The travelling speeds were (a) 20 mm/h; (b) 100 mm/h; (c) 500 mm/h; (d) 2000 mm/h; and (e) 3500 mm/h.

Table 1
Chemical composition (cation percentage). The errors in the experimental values are the maximum standard deviation between statistical values of the fitting procedure and the standard deviation of the averages among measurements on different sample positions.

	Ceramic	20 mm/h	100 mm/h	500 mm/h	2000 mm/h	3500 mm/h	Nominal composition
Al	70.2 ± 0.8	70.5 ± 0.4	70.0 ± 0.4	70.1 ± 0.4	69.8 ± 0.4	69.7 ± 0.4	69.90
Mn	0.76 ± 0.1	0.66 ± 0.1	0.76 ± 0.1	0.73 ± 0.1	0.76 ± 0.1	0.77 ± 0.1	0.762
Y	17.3 ± 0.4	17.3 ± 0.3	17.5 ± 0.3	17.2 ± 0.3	17.1 ± 0.3	17.5 ± 0.3	17.44
Zr	11.6 ± 0.9	11.5 ± 0.3	11.8 ± 0.3	11.9 ± 0.3	12.3 ± 0.3	12.0 ± 0.3	11.94

on top, through which the laser beam reached the sample. It is known that the use of non-oxidant atmospheres is necessary in order to obtain AYZ samples without gas inclusions.[17] We used a high power diode laser, radiating at $\lambda = 940 \pm 10$ nm, and whose shape in the focus was a 10-mm length line, around 1 mm wide. The length of the laser line spanned all the width of the sample surface, and travelled on top of it at a predefined travelling speed along the sample length. On the laboratory reference frame, it was the sample + furnace that moved, while the laser system was kept fixed. Travelling constant speeds from 20 to 3500 mm/h were used. We used power densities from 550 to 950 W/cm^2. Upon these processing conditions, a thin elongated drop of material is molten and resolidified at the surface. We can estimate cooling rates at the very surface on solidification from temperature measurements performed on the solidification of the eutectic Al_2O_3–YSZ, which has similar thermal behaviour and melting temperature, processed using the same equipment.[27] At 20 and 3500 mm/h the estimated maximum solidification rates are approximately 50 and 300 K/s, respectively.

After processing, the samples were cooled down to room temperature at a rate of 8 °C/min. In Fig. 1 we show the appearance of samples processed at two different rates, 20 and 2000 mm/h. The surfaces of processed ceramics were purple coloured and smooth. Samples processed at the lowest rates were dull whereas samples scanned at the highest travelling speeds were glossy as shown in Fig. 1. The sample borders are rounded due to the drop shape of the melt produced during the process. Surface roughness depends on the presence of gas bubbles into the processed layer and on the position of these into the processed layer. When bubbles are near the external surface, small protuberances are observed due to underlying bubbles; whereas when these are at the surface, craters can be seen on the surface. No one of those features are seen when processing at 20 mm/h, while whitish, small protuberances can be seen on the sample processed at 2000 mm/h, evidence of near-surface bubbles.

A longitudinal crack along the centre of the sample processed at 20 mm/h can be distinguished in Fig. 1. Samples cracked to some extent at all the solidification rates (see for example Fig. 2d and e). This is an indication that the thermal stresses suffered by the ceramic piece are still too large to completely avoid cracking. Although under the same processing conditions, Al_2O_3–YSZ eutectics are tough enough to resist cracking, the present material is less tough, and a larger preheating than the one used (1100 °C) would be needed to avoid any cracking. Our experimental equipment do not allow at present higher preheating temperatures at the same time that a protective nitrogen flow is blown to prevent the massive formation of gas bubbles.

At processing rates larger than 500 mm/h, gas bubbles form which end-up trapped in the resolidified layer. These can be better seen on transverse cross-section images. Fig. 2 shows optical cross-sections of the layers solidified at 20, 100, 500, 2000 and 3500 mm/h. The processed layers have thickness in the neighbourhood of 400 μm. The samples processed at 20 mm/h are free form bubbles. At 100 mm/h bubbles are very scarce. Only at the sample lateral position a large bubble (diameter larger than 100 μm) can be sometimes observed. At 500 mm/h large bubbles appear quite often, with diameters in cross-section around 100 μm, and are located more than 200 μm away from the ceramic substrate. Probably, very thin remelted (less than 100 μm) layers would be free of bubbles as long as the surface tension can be overcome to exit the surface layer. At the largest processing rates the bubbles are smaller but more frequent. A precise description of the amount of porosity and location of the bubbles is not easy on this material as the processing conditions affect them in different ways. First, the origin is dual: gas previously present into the ceramic (residual ceramic porosity) as well as gas from the surrounding atmosphere dissolved into the melt. Preventing both by processing fully dense ceramics and eliminating any soluble gas from the processing area would eliminate the bubbles completely. We have observed that using dry N_2 to process at atmospheric pressure, as we could do in our experiments, eliminates much of the bubble trapping into the solid. In fact, Oliete et al. found that this material could be grown as thin rods by LFZ on a N_2 atmosphere or under vacuum at pulling rates up to 1200 mm/h.[17] A second process, porosity

Table 2
Processing conditions (laser power density and travelling rate) and resultant remelted-layer and HAZ thicknesses.

Sample ref.	Power density (W/m)	Travelling rate (mm/h)	Processed layer thickness (μm)	HAZ thickness (μm)
A	5500	20	513	289 ± 4
B	6000	100	553	116 ± 4
C	6500	500	577	49 ± 4
D	7500	2000	450	22 ± 4
E	9500	3500	447	27 ± 4

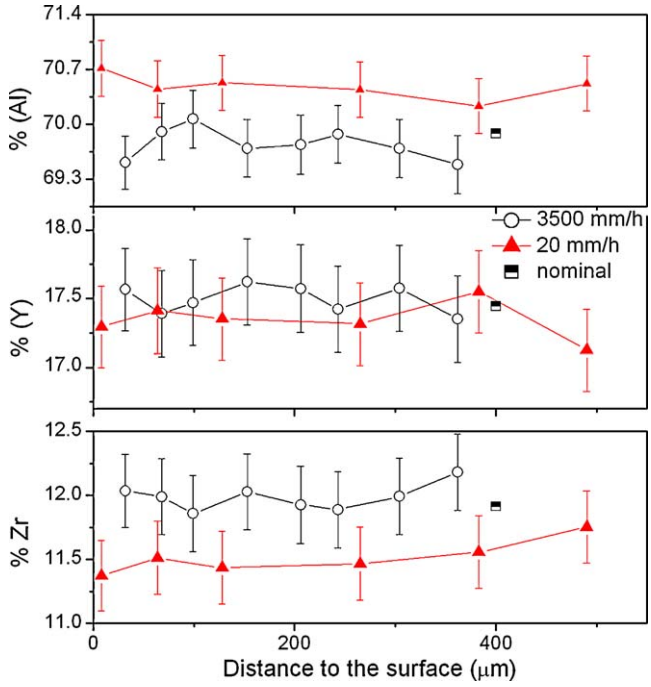

Fig. 3. Chemical composition (cations) of the remelted layer processed at 20 and 3500 mm/h as a function of the distance to the external surface.

coarsening into large bubbles and bubble travelling towards the hottest regions of the melt (assisted by convection currents), requires time to be effective in taking out the bubbles from the advancing solidification front towards the melt and eventually out to the atmosphere. This is why at very low processing rates no bubbles are left, as evolved gases have time to evolve towards the atmosphere during solidification. Third, time is also required to allow the dissolution of gases into the melt, this may explain why, at very large solidification rates, less total porosity seems to be left into the material.

4. Characterization results and discussion

The kind of processing presented is expected to be the most useful to modify the ceramic surface so as to make it dense, textured and with fine controllable microstructure. A microstructure which is stable and free from primary or segregated phases is important to prevent coarsening that would impair the good resistance to wear, erosion or chemical corrosion expected from the dense, composite nature. However, some reports on laser surface processed ceramics have shown chemical segregation towards the surface, especially at low processing rates.[28] We will characterize in the following the chemical, structural and microstructural features of the produced layers.

4.1. Chemical analysis

We have performed chemical analysis by EDS on transverse cross-sections of the layers under the scanning electron microscope, analysing the characteristic X-rays of the cations. In Table 1 we give the results for the average values inside the processed layers. We include also the measured composition of the initial ceramic. We can see that the chemical composition of the layer does not change upon laser processing. Only the amount of dopant, Mn, seems to diminish in the slow processed ceramic. Manganese oxides might evaporate while processing but still the measured amount stays inside the uncertainty limit

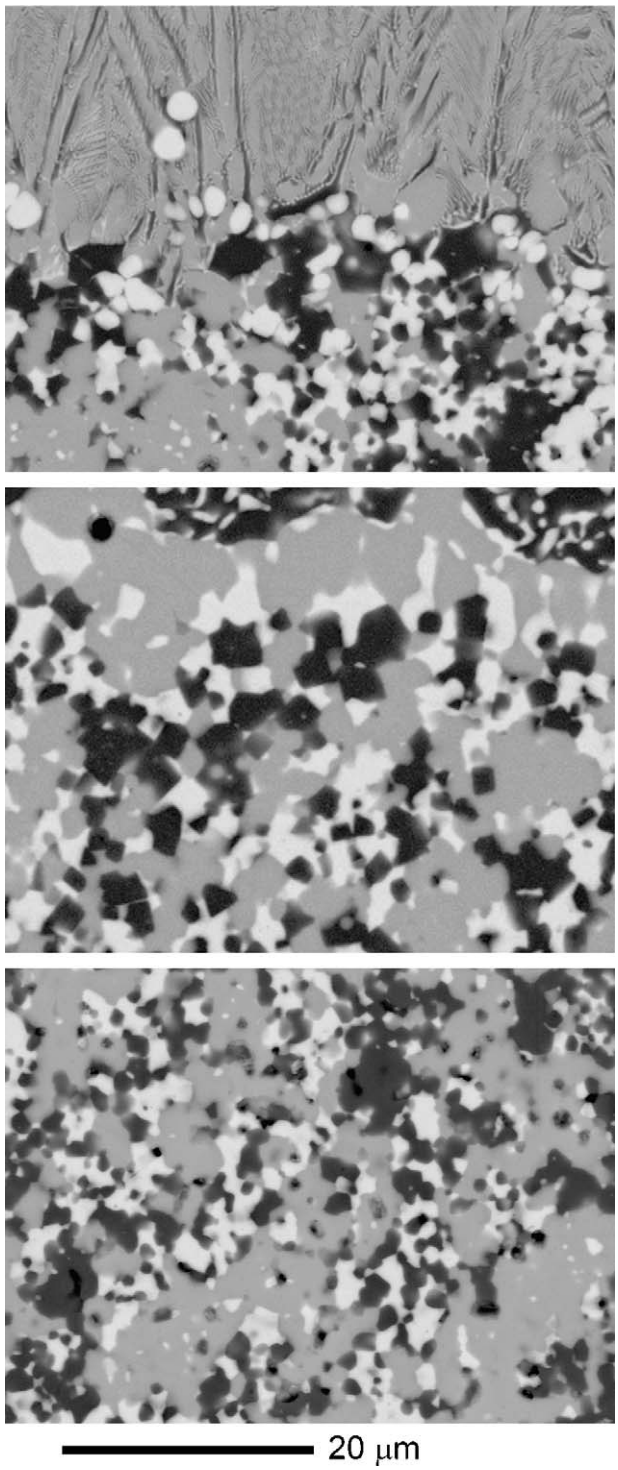

Fig. 4. (a) and (b) Scanning electron micrographs of the ceramic substrate near to the remelted layer (seen in the upper part of the respective micrograph). The travelling speeds were (a) 3500 mm/h and (b) 20 mm/h. (c) SEM micrograph of the ceramic. Images taken on transverse cross-sections cut perpendicular to the laser travelling direction.

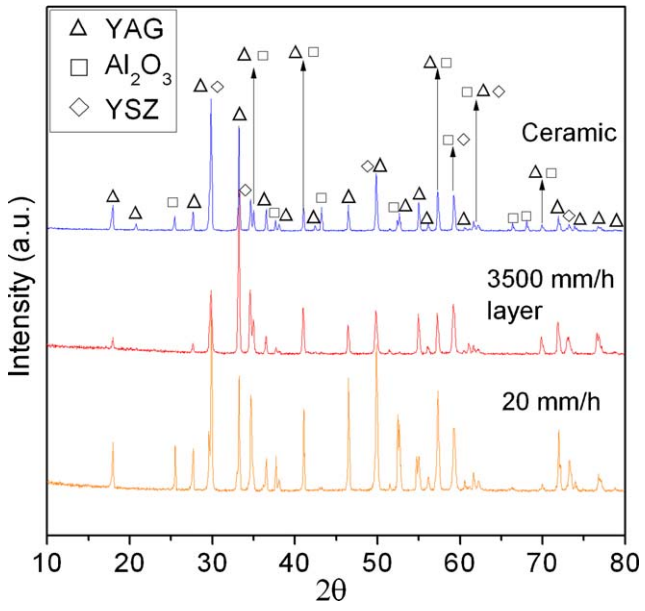

Fig. 5. X-ray powder diffraction diagram measured on the ceramic and on the processed layers, as indicated in the figure and in the text.

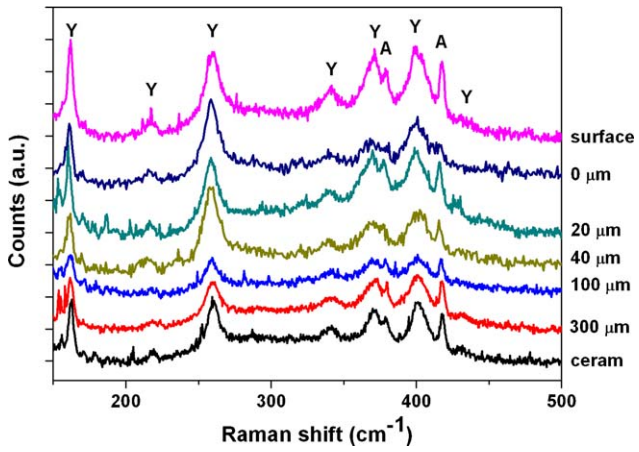

Fig. 7. Raman dispersion spectra measured at room temperature, in backscattering geometry on the surface (upper curve); on a transverse cross-section (cut perpendicular to the laser travelling direction) of a remelted layer processed at 3500 mm/h at different distances to the surface (as indicated on the figure); and on the ceramic substrate. A broad luminescence band has been subtracted from the spectra for clarity.

of the measurement. As observed in Fig. 3, the composition is also homogeneous all across the layers at all processing rates.

4.2. The heat affected zone

From the optical photographs of Fig. 2 we have measured the thickness of the processed layer at each processing condition. The data are collected in Table 2. The pictures in Fig. 2 also show different contrast inside the ceramic. The remelted layer is easy to distinguish as it is dense and opalescent at high solidification rates. Just below it the samples present a darker shade than the rest of the ceramic substrate. This region is a kind of heat affected zone (HAZ). Its thickness is also given in Table 2. It increases as the processing rate decreases. More specifically,

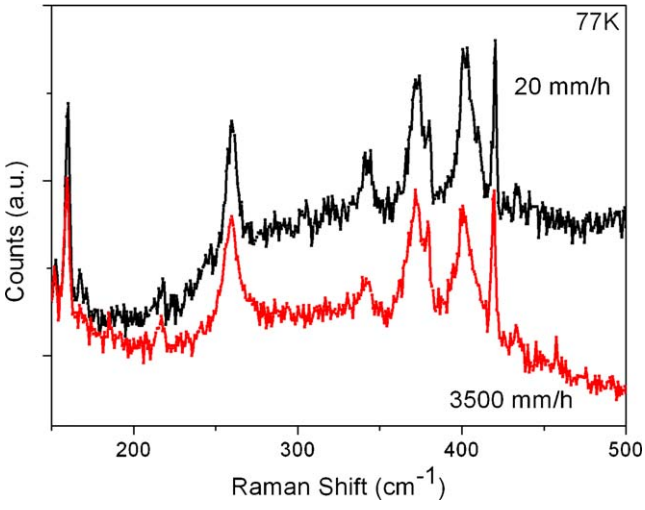

Fig. 6. Raman dispersion spectra measured at 77 K, in backscattering geometry. The Ar^+ 515 nm laser line was hitting the surface of the processed layers from above.

if we estimate the time during which the ceramic adjacent to the melt is surrounded by molten liquid (τ) as:

$$\tau = \frac{\text{processed-layer-thickness}}{\text{processing-rate}} \quad (1)$$

we can see that the HAZ thickness (t_{HAZ}) is proportional to sqrt(τ). This estimate of τ is reasonable as, to a good approximation, the length of the molten zone along the travelling direction is twice the thickness of the processed layer, being the latter easier to measure in the experiment. The linearity of t_{HAZ} vs. sqrt(τ) highlight some diffusivity from the molten area to be the rate determining process for the formation of the HAZ. Assuming t_{HAZ} equals to a diffusion length as $t_{HAZ} = 2\text{sqrt}(D\tau)$, we obtain a diffusion coefficient of 2×10^{-6} cm^2/s.

In a previous work on processing zirconia–alumina eutectics without preheating[29] it was observed that the microstructure of the material adjacent to the molten pool evolved in a layer of 8 μm when processing at 500 mm/h. In the present case, there is also some evidence by SEM of evolution of the microstructure adjacent to the molten area. Elimination of residual porosity can be inferred from the SEM micrographs and, at the lowest processing rates, also some coarsening of the microstructure (see Fig. 4), in areas adjacent to the melt. Consequently, it is reasonable to associate this change in optical appearance to the elimination of residual porosity, which may be expected as a consequence of the high temperatures at which the area has been subjected during processing. An increase in density would diminish light scattering and give less diffuse reflectance and consequently, a darker appearance than the surrounding ceramic on the optical micrographs. One cannot rule out contribution to this darker appearance of the formation of colour centres during processing, promoted by oxygen diffusion during the high temperature processing in N_2 out of the hottest areas.

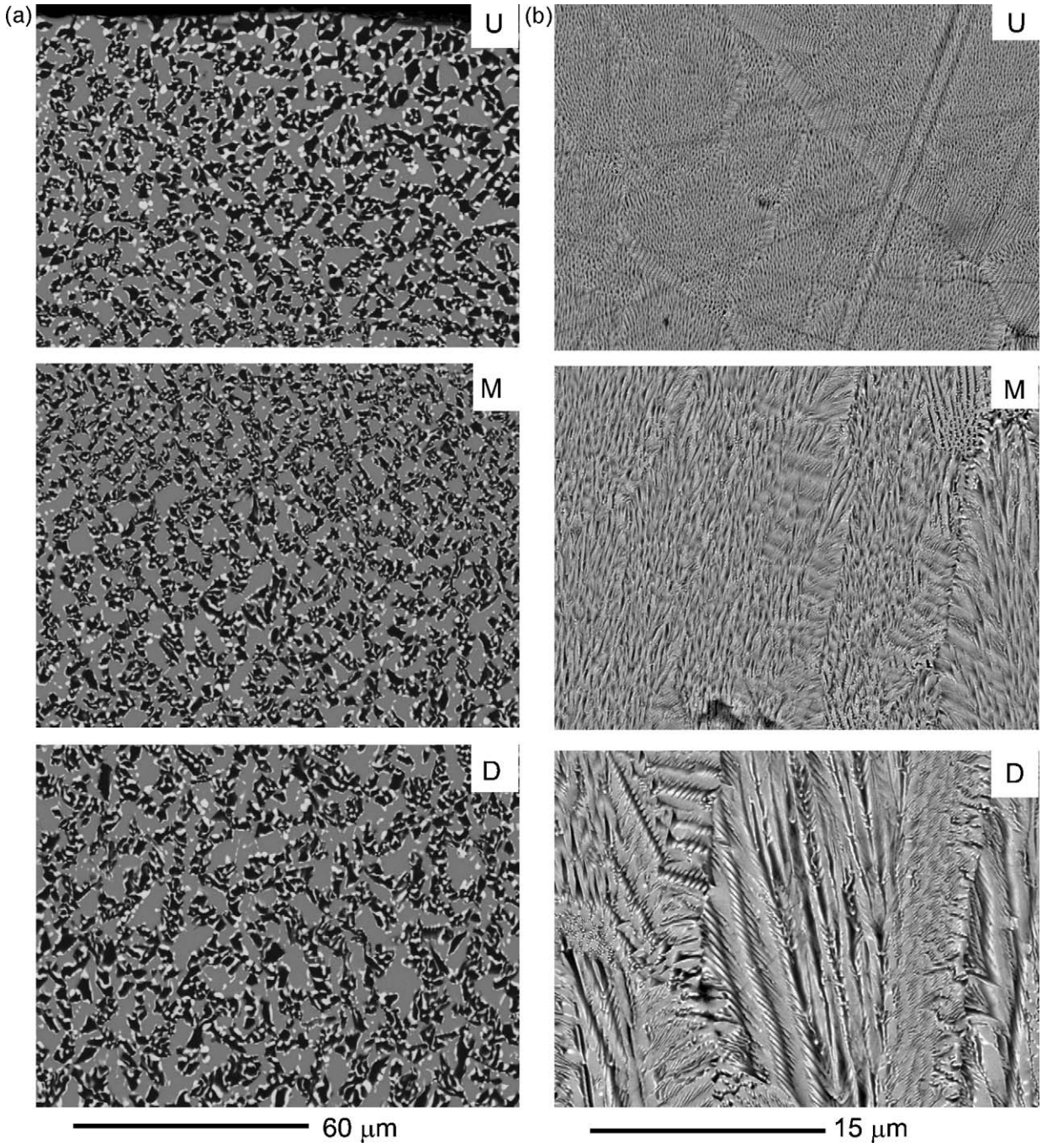

Fig. 8. SEM images of transverse cross-sections of layers processed at 20 mm/h (a, left) and 3500 mm/h (b, right). U, M and D label images taken near to the surface (U), in the middle of the layer (M), and near to the ceramic (D). The sample shown in (a) had a total remelted thickness of 450 μm and the images are centred at distances of (U) 40 μm, (M) 245 μm and (D) 380 μm from the surface; the sample shown in (b) had a total remelted thickness of 440 μm and the images are centred at distances of (U) 40 μm, (M) 200 μm and (D) 420 μm from the surface. The samples were cut perpendicular to the laser travelling direction to obtain the cross-sections.

4.3. Identification of phases: X-ray diffraction and Raman scattering

We have recorded X-ray diffraction powder patterns in bulk as-sintered and laser treated samples. The diffractograms are given in Fig. 5. The as-sintered ceramics were composed of crystalline α-alumina, YAG and cubic zirconia and there was no trace of the initial ceramic oxides Y_2O_3 or YSZ indicating that the chemical reaction had taken place upon sintering. The diffraction peaks correspond to crystalline α-alumina, YAG and cubic zirconia. At low growth rates (20 mm/h), the layer is textured, with some diffraction peaks absent ((220) at 20.9° and (4 4 0) at 42.6° from YAG and (1 0 $\bar{1}$ 4) at 35.1° and (1 1 $\bar{2}$ 3) at 43.34° from Al_2O_3). At 3500 mm/h, there is also evident texture. In this case, the underlying ceramic was eliminated prior to X-ray diffraction. (2 2 0) at 20.9°, (4 4 0) at 42.66, and (4 4 4) at 52.8°

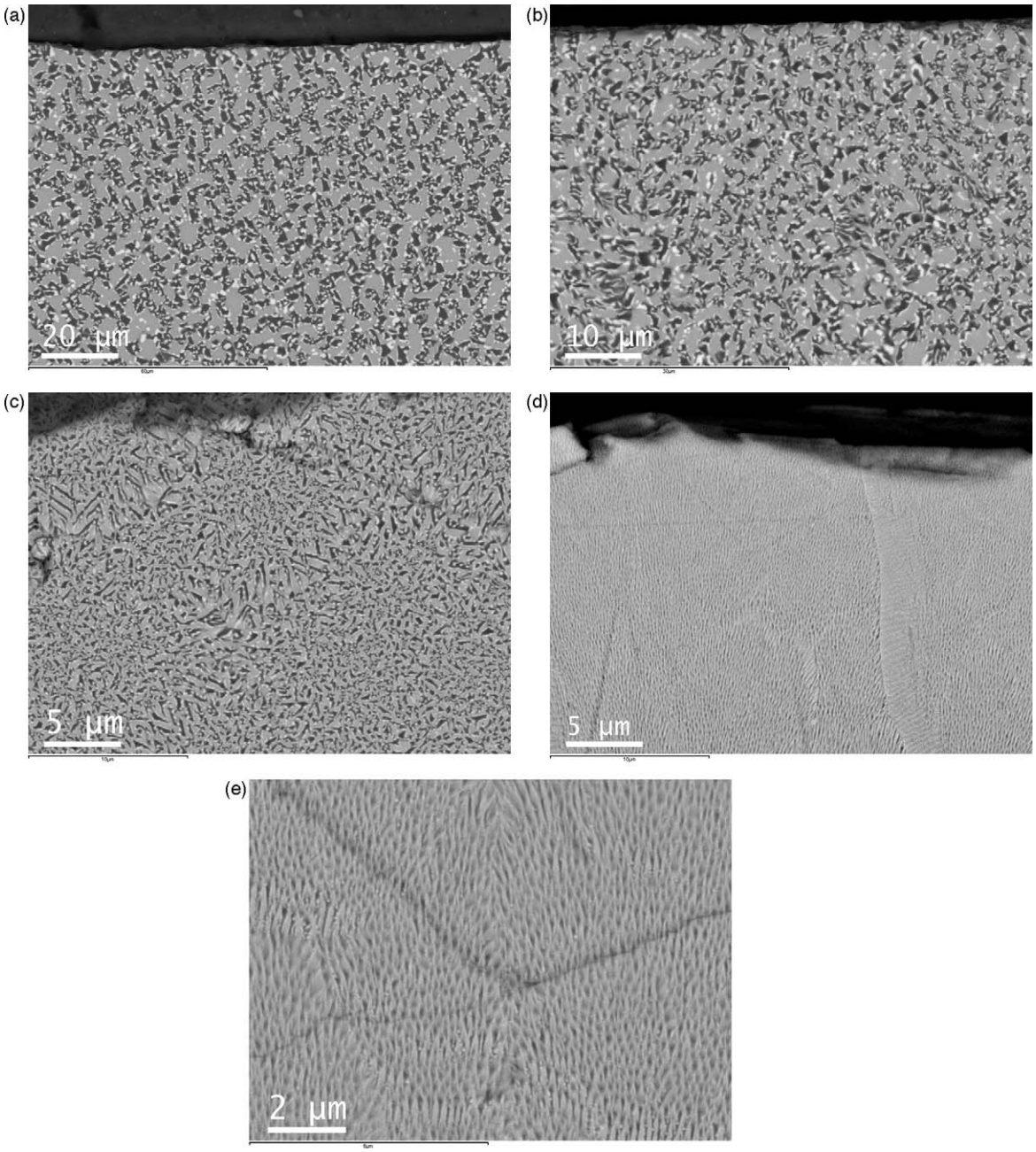

Fig. 9. Scanning electron micrographs of the transverse cross-section near the surface of laser processed specimens. The travelling speeds were (a) 20 mm/h; (b) 100 mm/h; (c) 500 mm/h; (d) 2000 mm/h; and (e) 3500 mm/h. Plane of the image cut perpendicular to the laser travelling direction.

diffraction peaks from YAG disappear and $(1\,0\,\bar{1}\,2)$ at 25.6°, $(1\,1\,\bar{2}\,3)$ at 43.34°, $(0\,2\,\bar{2}\,4)$ at 52.5° from Al_2O_3, while others, mainly (4 2 0) at 33.4° from YAG and (2 2 0) at 50.0° from YSZ have larger relative intensity. Evidently, this texture results from the dominant crystallographic growth directions of the composite and the curvature of the solidification front, which follows the melt-pool shape. There is no trace in the processed layers of other phases such as glass, or metastable crystalline phases as YAP ($YAlO_3$) that might form under conditions of fast cooling rates[30] or overheated melt.[31] Note that the maximum cooling rate estimated for the sample processed at 3500 mm/h is 300 K/s comparable to the ones used to obtain vitreous phases.

Raman spectroscopy confirmed the results obtained by X-ray diffraction. In Fig. 6 we give the Raman spectra taken on the surface of samples processed at 20 and 3500 mm/h at 77 K, in the range from 150 to 500 cm^{-1}. In both cases the Raman spectra show peaks due to YAG and α-Al_2O_3 superimposed onto the cubic zirconia band and a broad luminescence band, more visible outside the range shown. As the samples are partially transparent into the visible, we cannot be certain that the spectra shown in Fig. 6 correspond to the surface of each sample. To have a better spatial resolution we have recorded the Raman spectra on a transverse cross-section of the sample processed at 3500 mm/h at different distances form the surface. This is shown

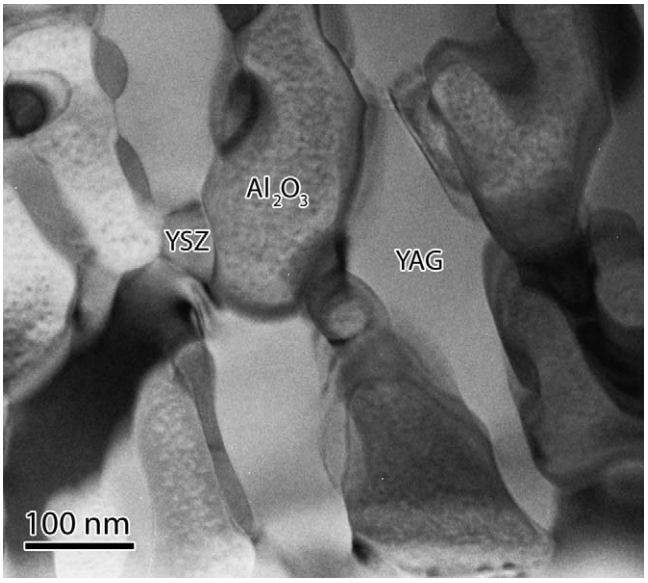

Fig. 10. TEM micrograph of the transverse cross-section near the surface of a specimen laser processed at 3500 mm/h.

in Fig. 7 at room temperature. Irrespective of the position on transverse cross-sections, the same Raman lines are observed, corresponding to YAG and Al_2O_3. Just at the surface (0 μm label in Fig. 7), a broadening of the Raman lines due to YAG and Al_2O_3 can be observed.

4.4. Microstructure

The microstructure of the processed layer is given in Figs. 8–11. Figs. 8 and 9 are SEM images of transverse cross-sections. Three different phases can be distinguished, corresponding to the ones detected by X-ray diffraction. The light phase is YSZ, the grey one corresponds to YAG and the dark one to Al_2O_3. No phases based on manganese oxides are seen, an indication that this dopant has been dissolved into the other phases. In Fig. 8 we give transverse micrographs of samples processed at 20 and 3500 mm/h at different positions inside the layer. The microstructure is eutectic across the cross-section, without segregated phases and with some change in the interphase spacing, increasing towards the inner of the layer on average. At travelling rates of 3500 mm/h, a marked directionality of the microstructure from bottom to top can be observed near to the underlying ceramic (Fig. 8bD), which is much less evident at low growth rates (Fig. 8aD). At low travelling rates, the phases grow parallel to the travelling direction (perpendicular to the page in the micrographs) at a depth of 40 μm from the outer surface (Fig. 8aU), and seem to keep some degree of directionality from bottom to top at faster solidification rates (Figs. 8bU and 9d, e), a consequence of the elongation of the melt-pool along the travelling direction as the travelling rate increases. At the interphase with the ceramic, the growth starts by nucleating a layer composed of YAG and YSZ at 20 mm/h (see Fig. 4b), while at 3500 mm/h, some zirconia primary rounded particles are formed (Fig. 4a).

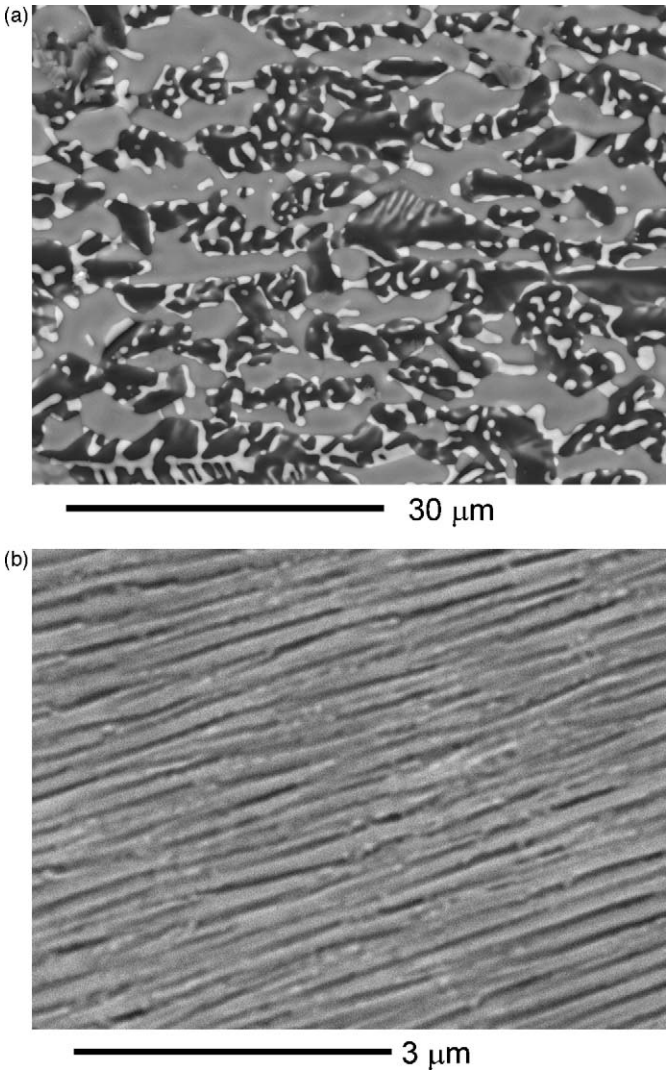

Fig. 11. SEM micrographs on the free surface of specimens laser processed at 20 mm/h (a) and 3500 mm/h (b). The scanning direction is horizontal.

The microstructure at the surface is the result of solidification nearly parallel to the surface, and then, takes place at a rate very close to the travelling rate. Representative micrographs of transverse sections of ternary eutectics AYZ grown at 20, 100, 500, 2000 and 3500 mm/h near the surface are shown in Fig. 9. We show micrographs of the subsurface areas where the microstructure is finer. The microstructure of the sample processed at 20 mm/h (Fig. 9a) shows three evenly distributed phases, Al_2O_3 (dark phase), cubic Y_2O_3-stabilized ZrO_2 (YSZ) (light phase) and YAG (grey phase). This microstructure is similar to the Chinese-script microstructure found in Al_2O_3–YAG eutectics, although less faceted and with the extra YSZ particles. The YSZ particles tend to be located at the Al_2O_3–YAG interfaces or dispersed into the Al_2O_3 phase, and are much smaller than the Al_2O_3 and YAG ones. At this low rate, the size of domains of YAG and Al_2O_3 are somewhat irregular. This interpenetrating microstructure is maintained at higher rates. At 100 mm/h, finer and coarser areas can be seen, more evident at 500 mm/h where the onset of colony formation can be guessed. Since it has been reported that eutectic AYZ does not produce a

Table 3
Size of the microstructure features.

Growth rate (mm/h)	Colony diameter (μm)	Interlamellar spacing (μm)	Intercolony thickness (μm)
20	N.A.	5.8 ± 3.6	N.A.
100	N.A.	2.5 ± 2.1	N.A.
500	16.3	0.5 ± 0.4	0.7
1000	8	0.4 ± 0.2	0.7
2000	7.7	0.3 ± 0.2	0.4
3000	5.5	0.3 ± 0.2	–

cellular microstructure up to very high growth rates, the cellular microstructure observed in Fig. 9 can be due to slight differences from the exact eutectic composition, or to the Mn_2O_3 doping. The YSZ domains cannot be resolved by scanning electron microscopy at higher growth rates, as in the samples grown at 2000 and 3500 mm/h (Fig. 9d and e) and again, a cellular microstructure is formed. In this case, the microstructure seems more elongated. This microstructure agrees with results reported by other authors.[10,19]

The interlamellar spacing was determined (average distance between equal phases) from Fourier transform analysis performed in transverse sections of the samples. Only areas near to the surface were analysed. The size of the colonies (when appropriate) and the width of the intercolony spacing have also been estimated from the images. Table 3 collects these microstructural-feature sizes. The faster the scanning rate the finer the interphase and intercolony spacing. Similar interphase spacings have been observed in samples fabricated by different methods and authors.[11,14,16] The dependence with the travelling rate follows only loosely the relationship $\lambda^2 V = \text{constant}$. This is not unreasonable as the microstructure morphology and growth conditions also change with pulling rate and moreover the actual solidification rate might not be the travelling speed at the fastest rates.

Image analyses of these transverse cross-section micrographs allow to quantify the volume fraction of each phase on the samples processed between 20 and 500 mm/h. At larger processing rates SEM micrographs do not have enough resolution to quantify. There is no measurable difference among the different solidification rates. At 20 mm/h we obtain 20.5 ± 1.0 vol.% zirconia, 39.2 ± 1.1 vol.% YAG and 40.3 ± 1.1 vol.% Al2O3. (Errors are standard deviations.)

To observe the fine microstructure at the fastest growth rate, TEM observations were made in the sample processed at 3500 mm/h. One such micrograph is presented in Fig. 10. The free surface of the processed sample is on the lower part of the image. Here, the YSZ phase is the darkest, Al_2O_3 the brightest and YAG is the grey one. It is clear that YSZ tends to be located as a thin layer separating YAG and Al_2O_3. The TEM observations confirm that there are no extra phases on these fine-microstructured regions. They also permit measuring the yttria amount dissolved into the yttria stabilized zirconia phase by EDS, giving YSZ phase with the composition in percent cations: 69 ± 6% Zr and 31 ± 6% Y; that is, 18.3 ± 3.2 mol% Y_2O_3 doped zirconia.

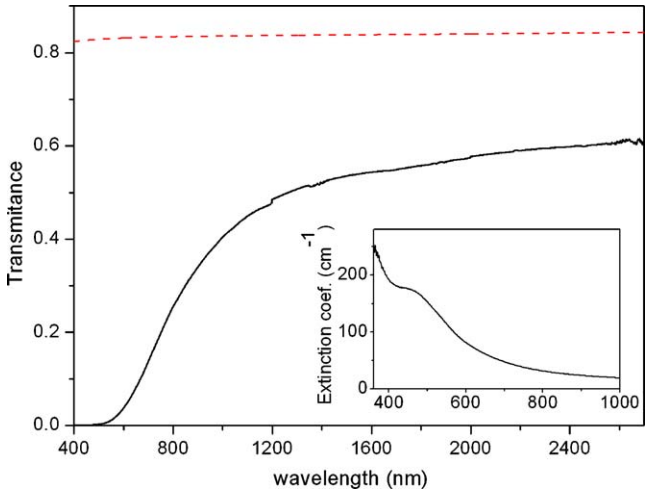

Fig. 12. In-line transmittance spectra of the layer processed at 3500 mm/h (380 μm thick). The dotted line is the theoretical transmittance of a pure slice of the same average refractive index (losses at the surface at normal incidence). The inset gives the extinction coefficient in the low wavelength range. The bump is due to the presence of Mn^{2+} ions dissolved in the component crystals.

Longitudinal SEM micrographs taken on the top surface of samples processed at the two extreme processing rates are shown in Fig. 11. The travelling direction goes horizontal to the images. In this figure it is clearly seen that the alignment of the microstructure is strong at the fast solidification rate. At slow solidification rates, although elongated along the solidification direction, the shape of each phase is more interpenetrating than aligned. Note that this coincides with what was observed in the transverse cross-sections and also observed by other authors. The important point is that the microstructure is the same, homogeneous and interpenetrating, as in the inside of the layers also at the very surface.

4.5. Optical transparency

The high density of the remelted material, free from interphase porosity or other phases, and the small size scale of the microstructure makes the large rate (3500 mm/h) processed samples translucent, as could be observed in Fig. 1. In fact, once the underlying ceramic has been taken out, the slab becomes partially transparent. The optical transmission spectra of a 382 μm thick slab for in-line propagation is given in Fig. 12 (continuous line). The discontinuous line gives the maximum theoretical transmission, that is, the transmittance of a slab of the same refractive index, non-absorbing and without scattering, calculated using the equation[32]

$$T = \frac{2n}{n^2 + 1}$$

where n is the refractive index. n has been estimated as an arithmetic average of the refractive indexes of the component materials, YSZ, YAG and Al_2O_3 (ordinary and extraordinary propagation), with dispersion relationships compiled by Tropf et al.[33] In the inset we give the extinction coefficient (after subtracting the reflection losses) in the low wavelength range. The

wide band around 480 nm is due to the presence of Mn^{2+} ions dissolved in the component crystals.

At long wavelengths the transmission levels off, reaching 60% at $\lambda > 2400$ nm, and 53% at $\lambda = 1500$ nm, 71% and 63% of the maximum theoretical transmission, respectively. This is worse than the transmission observed for fine grained, fully dense ceramics Al_2O_3,[34] tetragonal zirconia[35] or yttria[36] where light scattering at pores and at grain boundaries have been minimized. It is however comparable to the transmission of single phase, conventionally processed ceramics.[20,21] This ternary eutectic contains as majority phases Al_2O_3 and YAG, which have not very different refractive indexes (1.744 and 1.811 at 1500 nm, respectively) and are less than 200 nm thick, and a relevant amount (20.5 vol.%) of the minority phase cubic zirconia, with much larger refractive index ($n = 2.111$). This latter phase, dispersed as small particles (around 40 nm thick) are most probably responsible for most of the light scattering observed in this material. The small size allows translucency of the composite material, in the same way that the smaller the pores the more transparent the ceramic.[37] In some way, the small size of the cubic zirconia particles compensates the large volume percent of this phase concerning optical transparency, while the composite, fine-grained nature of the material renders it a very much increased strength, as reported in the literature.

5. Conclusions

We were able to prepare compositionally homogeneous $Al_2O_3/Y_2O_3/ZrO_2$ eutectic oxide layers by laser melting of the surface of preheated sintered ceramic plates of 7 mm × 25 mm. Laser power and atmosphere growth were selected to obtain samples with a directionally resolidified surface at maximum growth rates of 3500 mm/h and aiming at restricting bubble porosity formation to a minimum. Elongated and isolated pores could not be avoided at growth rates greater than 500 mm/h.

Below the resolidified layer, a thin heat affected zone is created, characterized by a slight increased densification and whose dimensions are smaller as the growth rate increased. X-ray diffraction and spatially resolved Raman spectroscopy identify the crystallographic phases as α-Al_2O_3, cubic ZrO_2 and YAG at all processing rates. TEM experiments further confirmed the absence of other phases even at the very fine-microstructured regions.

The composition of the layer is homogeneous. Its microstructure is Chinese-script like, formed by an interpenetrating network of Al_2O_3 (40 vol.%) and YAG (39 vol.%) domains of similar size with smaller YSZ (21 vol.%) domains located mainly at the Al_2O_3/YAG interfaces. The microstructure was made up of colonies at travelling speeds greater than 500 mm/h, which are elongated along the travelling direction, whose microstructural features (colony diameter, intercolony thickness and interlamellar spacing) decreased as the travelling speed increased.

The optical transparency of the fastest processed layer reached 60% transmittance at 2400 nm, for a 380 μm thick layer. This is worse than single-phase fully dense fine-grained ceramics, but competitive when composite, dense and tough ceramics are considered.

Acknowledgments

The authors thank Prof. V.M. Orera and J. Gurauskis for useful discussions and help with some experiments in the course of this work. Financial support from the Ministerio de Educación y Ciencia of Spain and The European Community FEDER program under grants MAT2006-13005-C03-01 and MAT2009-13979-C03-03 is gratefully acknowledged. FJE thanks the financial support of BSH. SEM and TEM experiments have been performed in Servicio de Microscopía Electrónica (Univesidad de Zaragoza). X-ray diffraction experiments have been performed in Servicio de Difracción de Rayos X (Universidad de Zaragoza).

References

1. Llorca J, Orera VM. Directionally solidified eutectic ceramic oxides. *Prog Mater Sci* 2006;**51**:711–809.
2. Waku Y, Sakuma T. Dislocation mechanism of deformation and strength of Al_2O_3–YAG single crystal composites at high temperatures above 1500 °C. *J Eur Ceram Soc* 2000;**20**:1453–8.
3. Llorca J, Pastor JY, Poza P, Peña JI, de Francisco I, Larrea A, et al. Influence of the Y_2O_3 content and temperature on the mechanical properties of melt-grown Al_2O_3–ZrO_2 eutectics. *J Am Ceram Soc* 2004;**87**:633–9.
4. Pastor JY, Llorca J, Salazar A, Oliete PB, de Francisco I, Peña JI. Mechanical properties of melt-grown alumina–yttrium aluminum garnet eutectics up to 1900 K. *J Am Ceram Soc* 2005;**88**:1488–95.
5. Sayir A, Farmer SC. The effect of the microstructure on mechanical properties of directionally solidified Al_2O_3/ZrO_2 (Y_2O_3) eutectic. *Acta Mater* 2000;**48**:4691–7.
6. Ochiai S, Ueda T, Sato K, Hojo M, Waku Y, Nakagawa N, et al. Deformation and fracture behavior of an Al_2O_3/YAG composite from room temperature to 2023 K. *Compos Sci Technol* 2001;**61**:2117–28.
7. Pastor JY, Poza P, Llorca J, Peña JI, Merino RI, Orera VM. Mechanical properties of directionally solidified Al_2O_3–ZrO_2 (Y_2O_3) eutectics. *Mater Sci Eng A-Struct Mater Prop Microstruct Process* 2001;**308**:241–9.
8. Larrea A, Orera VM, Merino RI, Pena JJ. Microstructure and mechanical properties of Al_2O_3–YSZ and Al_2O_3–YAG directionally solidified eutectic plates. *J Eur Ceram Soc* 2005;**25**:1419–29.
9. Pastor JY, Llorca J, Poza P, de Francisco I, Merino RI, Peña JI. Mechanical properties of melt-grown Al_2O_3–$ZrO_2(Y_2O_3)$ eutectics with different microstructure. *J Eur Ceram Soc* 2005;**25**:1215–23.
10. Peña JI, Larsson M, Merino RI, de Francisco I, Orera VM, Llorca J, et al. Processing, microstructure and mechanical properties of directionally-solidified Al_2O_3–$Y_3Al_5O_{12}$–ZrO_2 ternary eutectics. *J Eur Ceram Soc* 2006;**26**:3113–21.
11. Lee JH, Yoshikawa A, Fukuda T, Waku Y. Growth and characterization of $Al_2O_3/Y_3Al_5O_{12}/ZrO_2$ ternary eutectic fibers. *J Cryst Growth* 2001;**231**:115–20.
12. Oliete PB, Peña JI, Larrea A, Orera VM, Llorca J, Pastor JY, et al. Ultra-high-strength nanofibrillar Al_2O_3–YAG–YSZ eutectics. *Adv Mater* 2007;**19**:2313.
13. Pastor JY, Llorca J, Martin A, Pena JJ, Oliete PB. Fracture toughness and strength of Al_2O_3–$Y_3Al_5O_{12}$ and Al_2O_3–$Y_3Al_5O_{12}$–ZrO_2 directionally solidified eutectic oxides up to 1900 K. *J Eur Ceram Soc* 2001;**28**:2345–51.
14. Balda R, García-Revilla S, Fernández J, Merino RI, Peña JI, Orera VM. Near-infrared to visible up conversion of Er^{3+} in $CaZrO_3$/CaSZ eutectic crystals with ordered lamellar microstructure. *J Lumin* 2009;**129**:1422–7.
15. Krell A, Hutzler T, Klimke J. Transmission physics and consequences for materials selection, manufacturing, and applications. *J Eur Ceram Soc* 2009;**29**:207–21.

16. Serivalsatit K, Kouluoz BY, Kokuoz B, Ballato J. Nanograined highly transparent yttria ceramics. *Opt Lett* 2009;**34**:1033–5.
17. Oliete PB, Pena JI. Study of the gas inclusions in Al_2O_3–$Y_3Al_5O_{12}$ and Al_2O_3–$Y_3Al_5O_{12}$–ZrO_2 eutectic fibers grown by laser floating zone. *J Cryst Growth* 2007;**304**:514–9.
18. Calderon-Moreno JM, Yoshimura M. Al_2O_3–$Y_3Al_5O_{12}$(YAG)–ZrO_2 ternary composite rapidly solidified from the eutectic melt. *J Eur Ceram Soc* 2005;**25**:1365–8.
19. Su HJ, Zhang J, Cui CJ, Liu L, Fu HZ. Rapid solidification of Al_2O_3–$Y_3Al_5O_{12}$–ZrO_2 eutectic in situ composites by laser zone remelting. *J Cryst Growth* 2007;**307**:448–56.
20. Su H, Zhang J, Tian JJ, Liu L, Fu HZ. Preparation and characterization of Al_2O_3/$Y_3Al_5O_{12}$/ZrO_2 ternary hypoeutectic in situ composites by laser rapid solidification. *J Appl Phys* 2008;**104**:023511–7.
21. Su H, Zhang J, Liu L, Fu H. Microstructure and mechanical properties of a directionally solidified Al_2O_3/$Y_3Al_5O_{12}$/ZrO_2 hypoeutectic in situ composite. *Compos Sci Technol* 2009;**69**:2657–67.
22. Triantafyllidis D, Li L, Stott FH. Crack-free densification of ceramics by laser surface treatment. *Surf Coat Technol* 2006;**201**:3163–73.
23. Larrea A, de la Fuente GF, Merino RI, Orera VM. ZrO_2–Al_2O_3 eutectic plates produced by laser zone melting. *J Eur Ceram Soc* 2002;**22**:191–8.
24. Ester F, Merino RI, Orera VM, Martin A, Pastor JY, Llorca J. Surface modification by laser melting of eutectic ceramic oxides. In: Sudarshan TS, Jeandin M, editors. *Surface Modification Technologies – XXI*. 2008. p. 297–304.
25. Ester F, Merino RI, Pastor JY, Martin A, Llorca J. Surface modification of Al_2O_3–ZrO_2 (Y_2O_3) eutectic oxides by laser remelting: processing and wear resistance. *J Am Ceram Soc* 2008;**91**:3552–9.
26. Polotai AV, Foreman JF, Dickey EC, Meinert K. Laser surface processing of B_4C–TiB_2 eutectic. *Int J Appl Ceram Technol* 2008;**5**: 610–7.
27. F.J. Ester, thesis in preparation.
28. Merino RI, Peña JI, Orera VM. Compositionally graded YSZ–NiO composites by surface laser meeting. *J Eur Ceram Soc* 2010;**30**:147–52.
29. Merino RI, Peña JI, Orera VM, Larrea A, Sánchez-Herencia AJ. Resolidificación superficial de eutécticos Al_2O_3–YSZ asistida por laser. *Bol Soc Esp Ceram Vidrio* 2004;**43**:855–62.
30. Harada Y, Uekawa N, Kojima T, Kakegawa K. Fabrication of $Y_3Al_5O_{12}$–Al_2O_3 eutectic materials having ultra-fine microstructure. *J Eur Ceram Soc* 2008;**28**:235–40.
31. Yasuda H, Ohnaka I, Mizutani Y, Waku Y. Selection of eutectic systems in Al_2O_3–Y_2O_3 ceramics. *Sci Technol Adv Mater* 2001;**2**:67–71.
32. Casas J. *Óptica*. Zaragoza, Spain: Librería General; 1989.
33. Tropf WJ, Thomas ME, Harris TJ. Properties of crystals and glasses. In: Bass M, editor. *Handbook of optics: devices, measurements and properties*, vol II, 2nd Ed. Mc Graw-Hill, Inc.; 1995.
34. Apetz R, Van Bruggen MPB. Transparent alumina: a light scattering model. *J Am Ceram Soc* 2003;**86**:480–6.
35. Krell A, Klimke J, Hutzler T. Transparent compact ceramics: inherent physical issues. *Opt Mater* 2009;**31**:1144–50.
36. Serivalsatit K, Kouluoz BY, Kokuoz B, Ballato J. Nanograined highly transparent yttria ceramics. *Opt Lett* 2009;**34**:1033–5.
37. Peelen JGJ, Metselaar R. Light scattering by pores in polycrystalline materials: transmission properties of alumina. *J Appl Phys* 1974;**45**: 216–20.